

A Series of Zn(II) Terpyridine-Based Nitrate Complexes as Two-Photon Fluorescent Probe for Identifying Apoptotic and Living Cells via Subcellular Immigration

Dandan Liu,[†] Mingzhu Zhang,[†] Wei Du,[†] Lei Hu,[†] Fei Li,[†] Xiaohe Tian,^{*,†,§} Aidong Wang,[‡] Qiong Zhang,[†] Zhongping Zhang,[§] Jieying Wu,[†] and Yupeng Tian^{*,†}

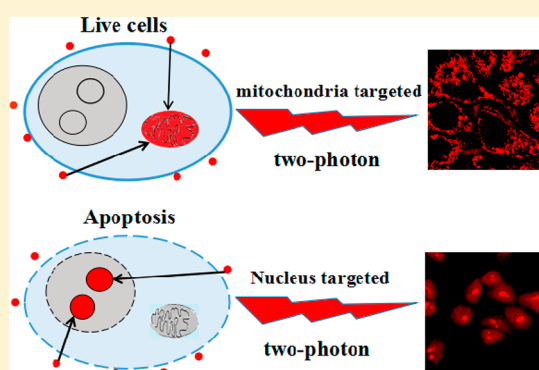
[†]Department of Chemistry, Key Laboratory of Functional Inorganic Material Chemistry of Anhui Province and [‡]School of Life Science, Anhui University, Hefei 230039, P. R. China

[‡]School of Chemistry and Chemical Engineering, Huangshan College, Huangshan, P. R. China

[§]School of Chemistry and Chemical Engineering, Anhui University, Hefei 230601, P. R. China

Supporting Information

ABSTRACT: Two-photon active probe to label apoptotic cells plays a significant role in biological systems. However, discrimination of live/apoptotic cells at subcellular level under microscopy remains unachieved. Here, three novel Zn(II) terpyridine-based nitrate complexes (C1–C3) containing different pull/push units were designed. The structures of the ligands and their corresponding Zn(II) complexes were confirmed by single-crystal X-ray diffraction analysis. On the basis of the comprehensive comparison, C3 had a suitable two-photon absorption cross section in the near-infrared wavelength and good biocompatibility. Under two-photon confocal microscopy and transmission electron microscopy, it is found that C3 could target mitochondria in living cells but immigrate into the nucleolus during the apoptotic process. This dual-functional probe (C3) not only offers a valuable image tool but also acts as an indicator for cell mortality at subcellular level in a real-time manner.



INTRODUCTION

Apoptosis, as a kind of programmed cell death, is vital for modulating various processes in cells. Signaling of such process occurred in different pathways, which, for example, include viscosity changes and DNA damage.^{1–4} Apoptosis exhibits several biochemical changes including cell lysis, the loss of mitochondrial electrochemical potential, and nuclear membrane damage that together result in various human conditions, such as immunodeficiency, ischemic damage, cancer, and neurodegenerative disease.^{5–8} Thus, real-time monitoring apoptosis might play a great important role in clinical diagnosis. Numerous fluorescent probes have been designed and synthesized for detection of apoptosis. Tan and co-workers utilized nanoparticle-based sensors to detect apoptotic cells due to the breaking of plasma membrane permeability and mitochondrial membrane permeability in early apoptosis.⁹ However, these nanoparticle-based sensors result in long synthesis process, large molecular weight, and low water solubility. He and co-workers have demonstrated an approach for the study of detection apoptosis upon induction of one-photon fluorescent probe;¹⁰ for that, the organic cationic compound could accumulate in mitochondria with normal MMP, and label the nucleolus in MMP vanishing cells due to its static interaction with DNA. However, the use of one-

photon probes has suffered from low penetration and photon damage as well as the autofluorescence, which were obstacles to their extensive use for imaging deep tissues and living bodies. Two-photon absorption (2PM) has been reported for deep penetration and avoiding autofluorescence of background, which is a promising approach to selectively detect apoptosis.^{11–14} Therefore, apoptosis-targeting 2PA probes containing optimized biocompatibility would be the ideal candidates for imaging apoptosis.

Recently, the use of metal complexes became an attractive approach for 2PM imaging. The metal complexes possessed unique merits:^{15–17} (1) energy-level process, which promote the electron transfer to enhance nonlinear optical (NLO) activity after coordinating with metal ions; (2) deep penetration and rapid response, which were important factors in bioimaging applications; (3) moreover, intense fluorescence and electron dense cores rendered them as dual-function imaging for 2PM microscopy and transmission electron microscopy (TEM).¹⁸ The merits of metal complexes were not only that they possessed a stronger NLO effect but also that they had potential bioimaging applications. Thereinto,

Received: March 14, 2018

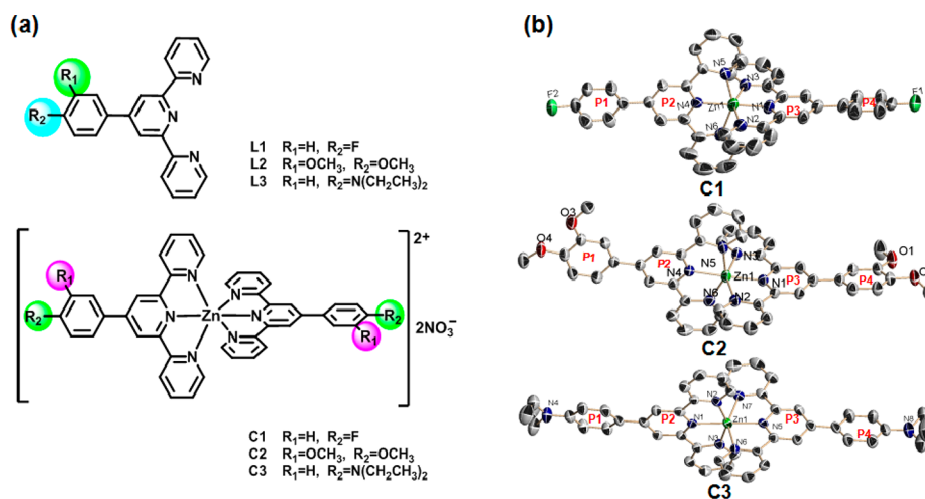


Figure 1. (a) The structures for all the compounds. (b) Crystal structures of C1–C3 (H and NO₃[−] were omitted, thermal ellipsoids at 50% probability).

zinc complex with considerable two-photon activity has drawn increasing attention.^{19–23} Because of their unique biocompatibility and less cytotoxicity, fluorescent zinc complexes could be ideal to monitor apoptosis, while offering stable signal and less invasiveness toward living cells. However, Zn²⁺ fluorescent probes with both 2PA activity and apoptosis specificity are scarcely reported according to our knowledge.

Spurred on by this, Zn-terpyridine complexes (C1–C3) obtained through self-assembly relied on the following merits (Figure 1a): (1) Different terminal substituents in the complexes can adjust the pull/push electronic capability of the molecule and achieve enhanced 2PA properties; (2) The metal Zn(II) was chosen as the central atom owing to its low cytotoxicity and cationic nature, which can make the complexes accumulate in the negatively charged mitochondria; (3) Nitrate ions in the zinc complexes further increased their solubility in water. As expected, Zn(II) complex C3 possessed excellent 2PA properties in the near-infrared (NIR) region and was applied for bioimaging application. 2PM imaging showed that C3 could be accumulated in negatively charged mitochondria^{24,25} and immigrated to the nucleolus in apoptotic cells due to increased nuclear membrane permeability. All these results suggest that C3 as a dual probe could be a promising candidate for targeting apoptosis in 2PM imaging.

EXPERIMENTAL SECTION

The synthetic procedures of the terpyridine ligands (L1–L3) and the relevant characterization data were listed in Supporting Information.

Synthesis of C1. L1 (0.46 g, 1.40 mmol) was dissolved in ethanol (50 mL), and Zn(NO₃)₂·6H₂O (0.21 g, 0.70 mmol) was added and then refluxed for 3 h. After it cooled to 25 °C it was filtered. The residue was purified by ethanol to give the product as a white solid (0.44 g, 74%). IR (KBr, cm^{−1}): 1614 (s), 1599 (s), 1516 (m), 1475 (m), 1432 (m), 1381 (s), 1228 (s), 1165 (s), 1015 (m), 844 (m), 793 (m), 571 (m). ¹H NMR (400 MHz, deuterated dimethyl sulfoxide (d₆-DMSO), ppm): δ 7.51 (m, 4H), 7.65 (t, 4H, J = 8.6 Hz), 7.96 (d, 4H, J = 4.4, 8.0 Hz), 8.30 (t, 4H, J = 7.6 Hz), 8.53 (m, 4H), 9.15 (d, 4H, J = 8.0 Hz), 9.40 (s, 4H). ¹³C NMR (100 MHz, d₆-DMSO, ppm): δ 116.47, 120.95, 123.52, 127.69, 130.66, 131.99, 141.31, 147.73, 149.46, 153.87, 163.00. Mass spectrometry (MS; matrix-assisted laser desorption ionization time-of-flight (MALDI-TOF)): m/z, calcd: 844.11. Found: 359.25 [M-2NO₃[−]]²⁺/2.

C2. Yield: 0.50 g (77%). IR (KBr, cm^{−1}): 3061 (w), 2937 (w), 2839 (w), 1589 (s), 1522 (s), 1474 (s), 1360 (s), 1263 (s), 1151 (m), 1017 (s), 796 (m), 763.80 (w), 603 (w). ¹H NMR (400 MHz, d₆-DMSO, ppm): δ 3.95 (s, 6H), 4.05 (s, 6H), 7.33 (d, 2H, J = 8.6 Hz), 7.51 (m, 4H), 7.94 (m, 6H), 8.05 (d, 2H, J = 8.5 Hz), 8.29 (t, 4H, J = 7.5 Hz), 9.15 (d, 4H, J = 8.1 Hz), 9.31 (s, 4H); ¹³C NMR (100 MHz, d₆-DMSO, ppm): δ 55.98, 111.79, 120.35, 121.66, 123.49, 127.68, 141.23, 147.77, 149.32, 151.62, 155.33. MS (MALDI-TOF): m/z, calcd: 928.26. Found: 401.10 [M-2NO₃[−]]²⁺/2.

C3. Yield: 0.54 g (81%). IR (KBr, cm^{−1}): 3060 (w), 2969 (w), 2927 (w), 1588 (s), 1531 (m), 1472 (m), 1353 (s), 1212 (m), 1155 (m), 1016 (m), 790 (m), 682 (m). ¹H NMR (400 MHz, d₆-DMSO, ppm): δ 1.19(m, 12H), 3.54 (q, 8H, J = 6.9 Hz), 6.92 (t, 4H, J = 14.6 Hz), 7.48 (dd, 4H, J = 5.5, 7.1 Hz), 7.91 (d, 4H, J = 4.8 Hz), 8.25 (m, 4H), 8.36 (m, 4H), 9.03 (d, 4H, J = 8.1 Hz), 9.22(d, 4H, J = 27.1 Hz). ¹³C NMR (100 MHz, d₆-DMSO, ppm): δ 12.48, 44.71, 111.75, 118.07, 122.73, 127.55, 129.73, 141.35, 146.84, 150.00. MS (MALDI-TOF): m/z, calcd: 950.38. Found: 412.17 [M-2NO₃[−]]²⁺/2.

RESULTS AND DISCUSSION

Crystal Structure Description. Structures of Ligands. As shown in Figure S1, the single-crystal structures of L2 and L3 have been reported in the literature,^{26,27} the ligands L1 and L3 crystallized in monoclinic system with P2₁/c space group; L2 belonged to triclinic system with P $\bar{1}$. The dihedral angle between P1 and P2 was 6.31° in L1, 7.43° in L2, and 5.04° in L3. The excellent planarity suggested that L3 was conducive to a better delocalized π -electron system.²⁸

Structures of Zn(II) Complexes. Crystals of C1 and C2 belonged to triclinic with P $\bar{1}$ space groups, and for C3, it was monoclinic system with P2₁/c space group (Table S1). Compared with the free ligands, the complexes displayed the expected octahedral geometry with two terpyridine ligands and one central Zn atom.²⁹ Because of the steric demand of the ligands, the N–Zn–N angles in the complexes were within the 75.01–76.01° range, deviating from the idealized values of 90° (Table S2). Furthermore, the dihedral angle between P4 and P3 followed the order of C1 (12.44°) > C3 (11.55°) > C2 (8.00°), revealing that there is a distinct substitute change in the terminal substituent for the terpyridine moiety of the complexes with subtle effect on their dihedral angles (Figure 1b). As expected, the structural characteristics had a great impact on the optical performance and 2PA response.

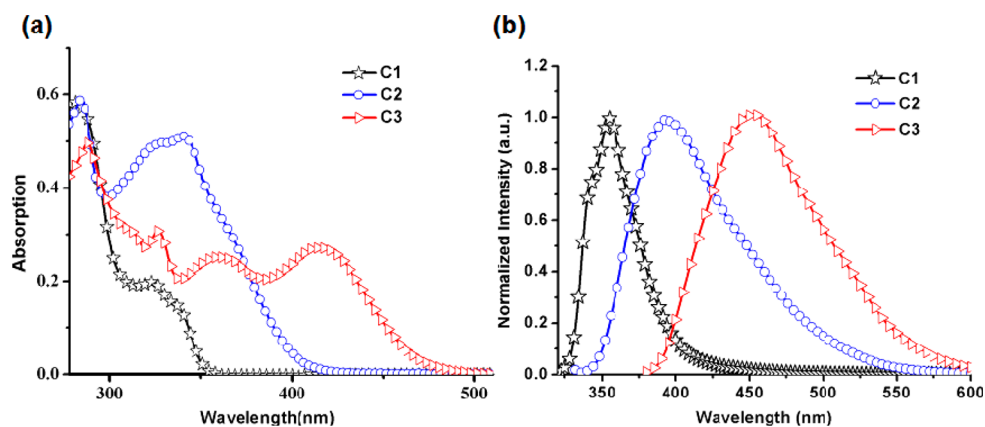


Figure 2. UV-Vis absorption (a) and normalized fluorescence (b) spectra for C1–C3 in benzene ($c = 10 \mu\text{M}$).

Optical Properties. The UV-vis absorption spectra of the complexes were presented in Figure 2a, and the complexes present three absorption bands. The absorption bands at 280–295 nm could be assigned to the π - π^* transition.³⁰ The absorption bands located at 327–356 nm were attributed to the intramolecular charge transfer (ICT) transition, and the absorption band at 417 nm was assigned to the metal-to-ligand charge transfer (MLCT), which was further proved by time-dependent density functional theory (TD-DFT).

The low-energy bands of C1 and C2 were calculated at 328 and 341 nm (corresponding to the highest occupied molecular orbital (HOMO) \rightarrow lowest unoccupied molecular orbital (LUMO+1) and HOMO-1 \rightarrow LUMO, respectively), which might be ascribed to the ICT and mixed with the ligand-to-ligand charge transfer (LLCT) transition (Figure S3). The high-energy bands (280–290 nm) were assigned to the $\pi_{\text{terpyridine}}-\pi^*_{\text{terpyridine}}$ transitions (HOMO \rightarrow LUMO in C1, HOMO-1 \rightarrow LUMO+1 in C2). In addition, the C3 presented a little different transition features (Figure S3c), the high-energy band ($\lambda_{\text{max}} = 294 \text{ nm}$) was assigned mainly to the $\pi_{\text{terpyridine}}-\pi^*_{\text{terpyridine}}$ transition due to the HOMO-1 \rightarrow LUMO+1. And the moderate bands at 327 and 356 nm (corresponding to the HOMO-1 \rightarrow LUMO+2 and HOMO \rightarrow LUMO+2, respectively), correspond to the ICT mixed with the LLCT transition. Moreover, the low-energy peak at 417 nm was attributed to the MLCT transition (HOMO-2 \rightarrow LUMO). In general, the TD-DFT calculations could offer reasonable explanation for their experimental absorption bands.

The maximal absorbance bands and the fluorescence peaks of the complexes in benzene presented a remarkable red shift in the sequence of C1 < C2 < C3 (Figure 2), which could be attributed to the electron-pushing strength of the end group in the complexes correspondingly: $\text{N}(\text{CH}_2\text{CH}_3)_2 > \text{OCH}_3 > \text{F}$. Meanwhile, TD-DFT of the Zn(II) complexes at low-energy peaks were 3.72 eV (C1), 3.58 eV (C2), and 2.97 eV (C3), respectively, giving an approving explanation on the red-shift phenomenon from C1 to C3.

Nonlinear Optical Properties (NLO). Given that there was a weak fluorescent emission for C2 and C3 in dimethyl sulfoxide (DMSO; Figure S4), the third-order nonlinear optical properties of the compounds were measured by open-aperture Z-scan technique.^{31,32} An obvious enhancement of σ values was observed from ligands to the Zn(II) complexes (Figure 3), which was attributed to the extension of the conjugation length. Besides, the order of the maximum σ values of the

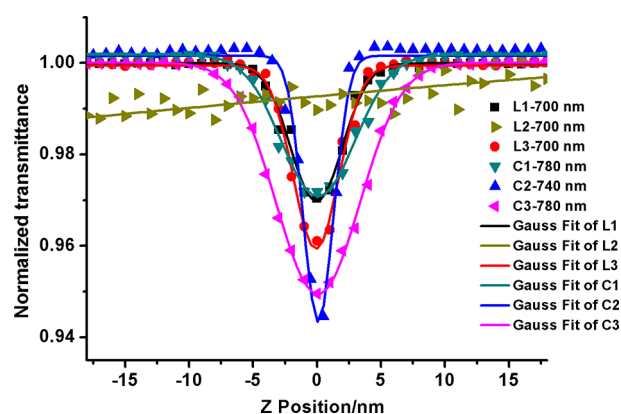


Figure 3. Z-Scan data for L1–L3 and C1–C3 ($c = 10 \mu\text{M}$) in DMSO. The solid curve is the theoretical fitting, and the dots are the experimental data.

complexes C1–C3 is C1 (709 GM) < C3 (1068 GM) < C2 (1260 GM). It can be explained that the planarity of the complexes will be different due to the coordination with the different ligands and that the good planarity will benefit to enhance the ability of charge transfer, thus increasing the two-photon absorption properties. This conclusion is highly in agreement with the results from both crystal structures and Lippert–Mataga plots (Table S3 and Figures 1 and S5).

Subcellular Location of C3 in Living Cells and Its Immigration during Apoptosis. As depicted in Figure S6, the low toxicity in living cells enables the compounds (L2, L3, C2, C3) as prominent fluorescent probes. Since C3 had excellent comprehensive photophysical optical properties, as well as a larger σ value in the longer excitation wavelength, which increased the penetration depth, C3 was subsequently used to test the capability of cellular location. As shown in Figure S7, C3 exhibited fibrillar luminescence in the cytosol, and no luminescence was observed in the nucleolus. To further determine the initial subcellular location of C3, the colocalization experiments with C3 and various organelle markers (Mito-tracker, ER-tracker, Lyso-tracker, and Nuc-red) were performed (Figure 4a). 2PM images strongly suggested that C3 targeted the intracellular mitochondria (Pearson correlation coefficient $R_r = 0.86$), which was also confirmed via processed fluorescence intensity profiles (Figure 4b). The affinity of C3 toward mitochondria was not unexpected, since its cationic nature might render the binding with subcellular compartment with high membrane potential.

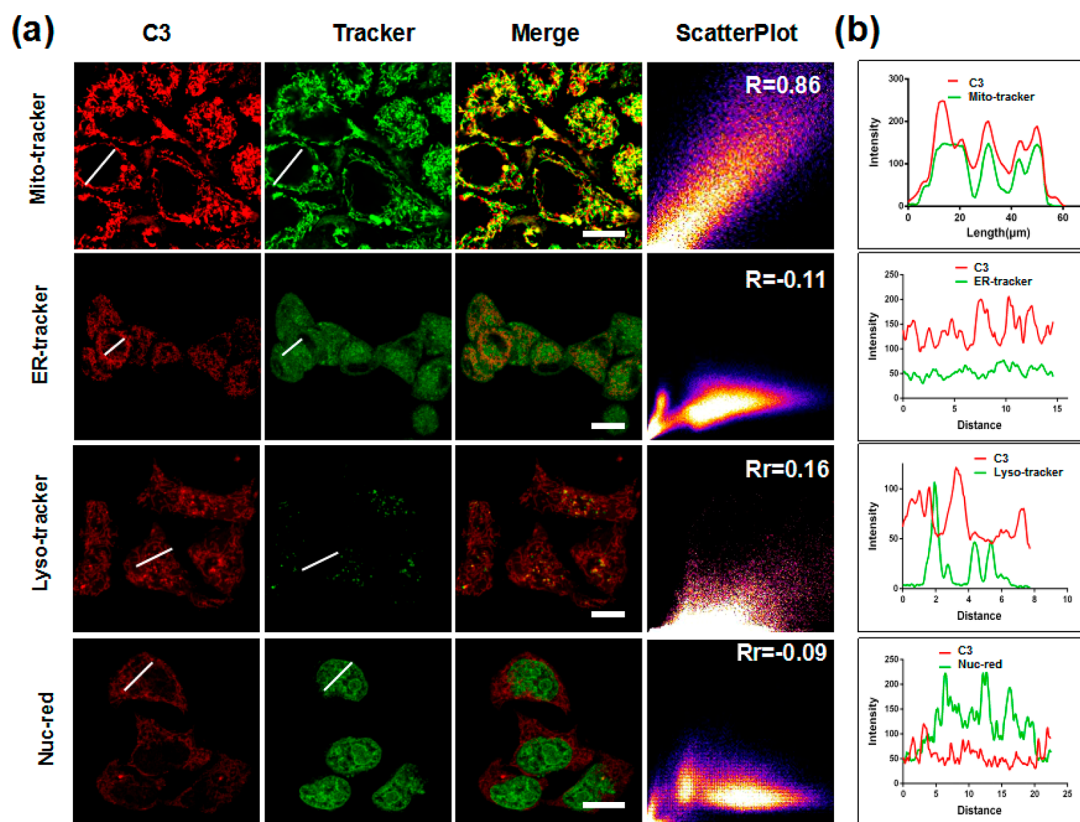


Figure 4. (a) Determination of subcellular localization of C3 under 2PM. HeLa cells were incubated with C3 ($\lambda_{\text{ex}} = 720 \text{ nm}$, $\lambda_{\text{em}} = 450\text{--}480 \text{ nm}$) for 20 min and coincubated with Mito-tracker (MitoTracker Red FM, $\lambda_{\text{ex}} = 580 \text{ nm}$, $\lambda_{\text{em}} = 590\text{--}620 \text{ nm}$) for 20 min, ER-tracker (ER-Tracker red, $\lambda_{\text{ex}} = 588 \text{ nm}$, $\lambda_{\text{em}} = 600\text{--}625 \text{ nm}$) for 20 min, Lyso-tracker (LysoTracker Red, $\lambda_{\text{ex}} = 576 \text{ nm}$, $\lambda_{\text{em}} = 580\text{--}610 \text{ nm}$) for 20 min, and Nuc-red (NucRedLive647, $\lambda_{\text{ex}} = 647 \text{ nm}$, $\lambda_{\text{em}} = 650\text{--}670 \text{ nm}$) for 10 min, respectively. The scale bars represent $20 \mu\text{m}$. (b) The fluorescence intensity profiles of C3 and trackers.

Intriguingly, at a starvation pretreated group (serum-free condition) from Figure 5a, while the cells partially underwent apoptosis, stronger signals in the whole nucleus were found within the apoptotic cells, which were extremely swollen and misshaped in bright-field micrographs. Since apoptosis was accompanied by increased permeability of the nuclear membrane and disappearance of mitochondrial membrane potential, it might cause the C3 migration from mitochondria to nucleus and “turn-on” the fluorescence upon nuclear acid binding.

To further confirm that C3 accumulated in mitochondria when the cells were alive and immigrated to nucleolus during apoptosis, apoptotic cells triggered by classic inducer was performed.³³ As shown in Figure S8, Live/Dead assays with Syto9 (a commercial living cells dye) and propidium iodide (PI, a commercial cells dye) again confirmed that C3 targeted the mitochondria in live cells. However, as displayed in Figure 5b, the fluorescence of C3 in drug-induced cells (5-Fu, cisplatin) was well-colocalized with that of PI, which demonstrated that C3 exhibited excellent nucleolus-targeting abilities that are attributable to the increased permeability of the nuclear membrane during apoptosis.³⁴ The results verified our design idea and implied the distribution of C3 relocated from mitochondria to nucleolus during apoptosis. Furthermore, the targeting capability of C3 in Triton-x100 treated cells and the fixed HeLa cells were well-consistent with the drug-induced cells,³⁵ further demonstrating that disrupted mitochondrial membrane potential and increased nuclear membrane permeability leads to the transfer of C3 from

mitochondria to nucleolus. During Triton-permeabilization and classic paraformaldehyde fixation (Figure S9) the whole cells was immobilized, and C3 displayed stronger signal than that in apoptotic cells. It is noteworthy that the bright circular signal within apoptotic cell nucleus might correspond to nucleolus, which mainly consists of negatively charged RNA. This implied that C3 in apoptotic cells may target nuclear RNA. As RNA also abundantly exists in mitochondria and nucleolus, it also might imply that the binding substance of C3 in living and fixed cells is mitochondrial and nucleolar RNA.

In addition to 2PM results, transmission electron microscopy (TEM) image of C3 was performed to confirm cellular distribution. As shown in Figure 6a, C3 in nontreated cells displayed abundant cylinder-like structures in the cell cytosol, highly corresponding to the mitochondria. In contrast, HeLa cells incubated with C3 and pretreated with 5-Fu presented reduced contrast in cytosolic regions with a large number of vacuoles, a classic symbol of early apoptosis, while significantly greater contrast was detected in the nucleolus (Figure 6b). This observation strongly supported our previous hypothesis that the intracellular immigration of C3 is from mitochondria to RNA-rich nucleolus.

It is interesting to note that C3 stained mitochondrial displayed a significant contrast within inner-membrane matrix (Figure 6c), while compared to mitochondria treated solely with osmium tetroxide (Figure 6d), a membrane electron microscopic agent, indicated much less contrast in inner-membrane matrix (Figure 6e). This again suggested C3 is

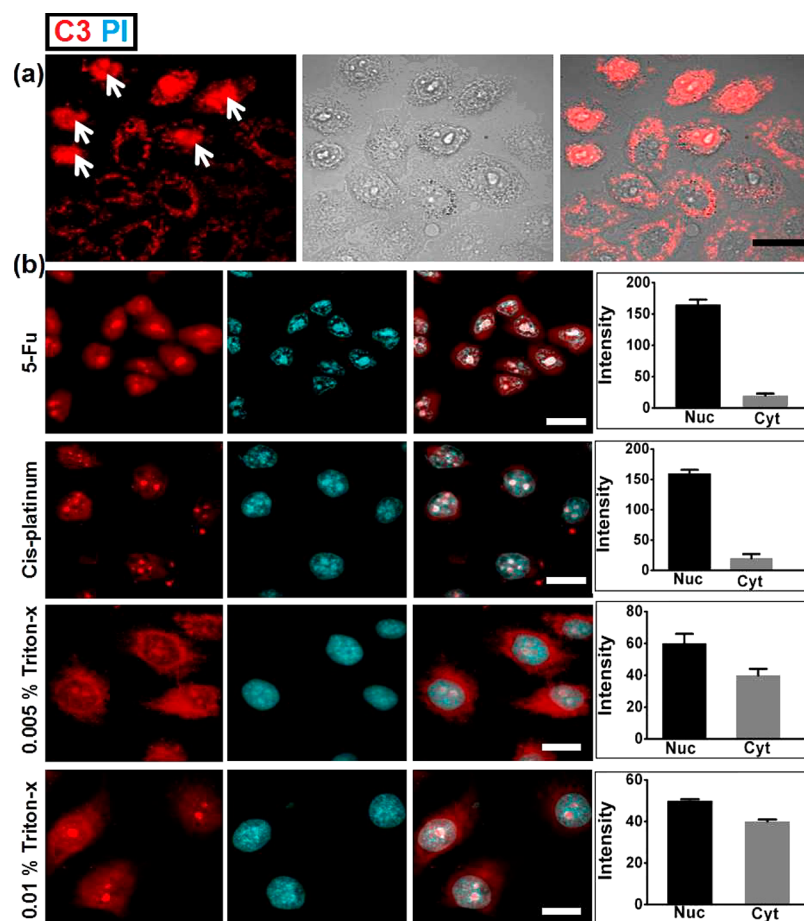


Figure 5. (a) HeLa cells starvation treated for 12 h and then stained with C3. White arrows identify the apoptotic cells in the culture. (b) Treatment with the apoptotic stimulants 5-Fu (5-fluorouracil), cis-platinum, and Triton-x100 then stained C3 and costain PI ($\lambda_{\text{ex}} = 493 \text{ nm}$, $\lambda_{\text{em}} = 620\text{--}640 \text{ nm}$). Scale bar = $20 \mu\text{m}$, and the relative fluorescence intensity of Cyt (cytoplasmic) and Nuc (nucleus) in HeLa cells after apoptosis-induced treatment.

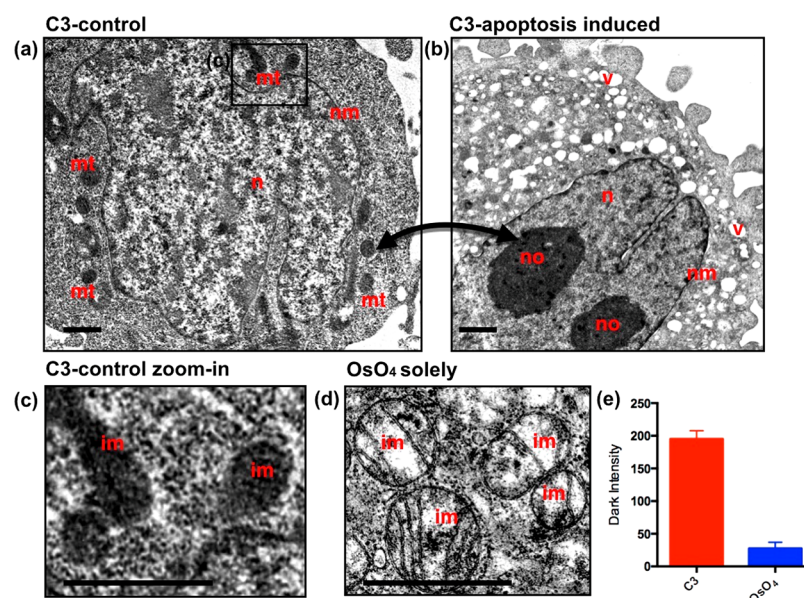


Figure 6. (a) TEM micrograph of live HeLa cells incubated with C3. (b) 5-Fu induced apoptotic cells incubated with C3. (c) Enlarged TEM micrograph from selected regions from (a) showing inner-membrane matrix. (d) Untreated HeLa cells solely stained with osmium tetroxide clearly showed bilayer mitochondria and less contrasted inner-membrane matrix. The scale bar represents $5 \mu\text{m}$. Abbreviations: mt = mitochondria, n = nuclear, no = nucleolus, nm = nuclear membrane, im = inner-membrane matrix, v = vesicles.

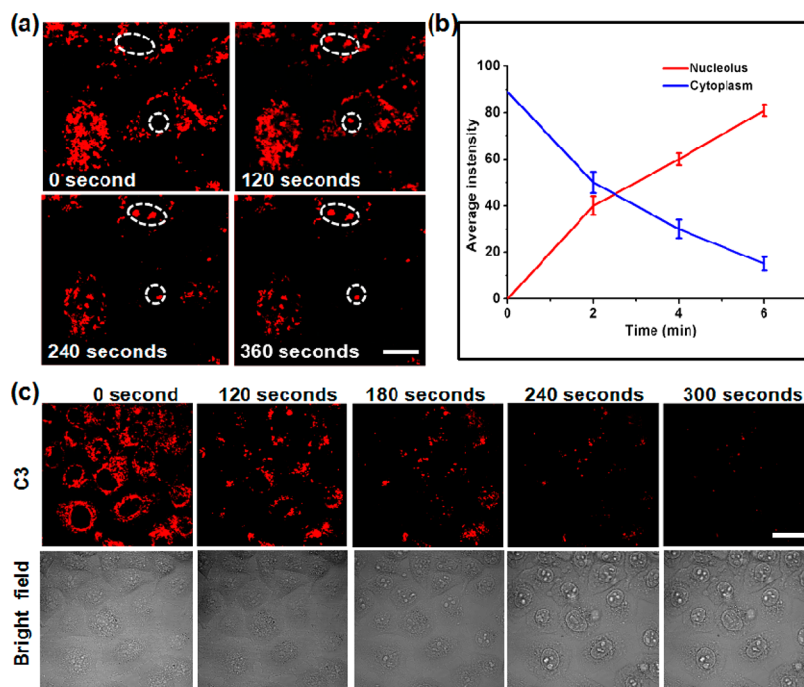


Figure 7. (a) The real-time monitoring images of HeLa cells intracellular fluorescence of C3 after treatment with H_2O_2 . (b) Plot of fluorescence intensity obtained from (a). (c) The real-time monitoring images of HeLa cells intracellular fluorescence of C3 after treatment with CCCP. Scale bar = $20\ \mu\text{m}$.

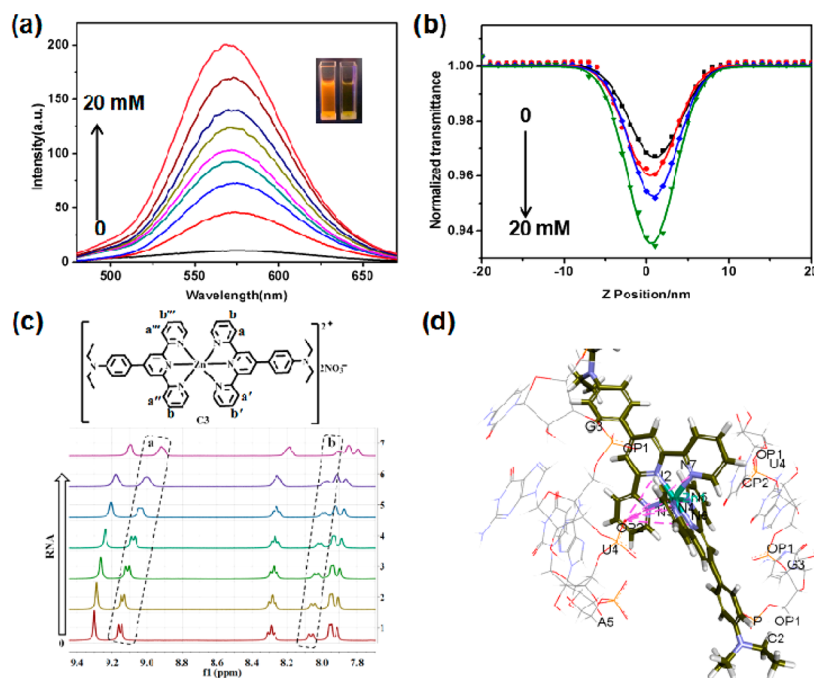


Figure 8. (a) Fluorescence spectral changes of $5\ \mu\text{M}$ C3 with 20 mM RNA. (b) Z-Scan data for $5\ \mu\text{M}$ C3 with 20 mM RNA. (c) ^1H NMR titration change for C3 + RNA in D_2O . (d) Models obtained after molecular modeling for the interaction of C3 with RNA fragment.

actually capable of penetrating mitochondrial bilayer membrane and targeting matrix RNA.

The Real-Time Imaging of C3 Subcellular Immigrating. Taking advantage of the applicability to real-time imaging, C3 was applied to investigate intracellular distribution during apoptosis induced by H_2O_2 . The live HeLa cells were initially stained with C3, and the fluorescence intensities were collected (Figure 7 and Supporting Information movie). 2PM imaging results showed that, before adding H_2O_2 , no obvious change in

cell morphology was observed and that mitochondrial signal was successfully obtained. After the extension of H_2O_2 treatment time, the cells showed shrinking morphologic changes as well as an attenuated fluorescence of mitochondria and an increased fluorescence of nucleolus (Figure 7a). After $\sim 360\ \text{s}$, the maximum fluorescence intensity was observed in nucleolus. In general, the nuclear membrane permeability was increased with the extension of the treatment time by H_2O_2 , resulting in more C3 probes being transported to the

nucleolus. At the same time, these significant changes in intracellular fluorescence with H_2O_2 time indeed matched well with the average fluorescence intensity of the linear region across the cells (Figure 7b). The sharp difference in fluorescence responses between the live and apoptotic cells highlighted the specificity and sensitivity of the C3 probe in detecting cell mortality in a real-time manner. Similar results were observed with CCCP-treated (to decrease mitochondrial membrane potential) apoptosis process (Figure 7c); with the extension of CCCP treatment time, C3 could no longer accumulate in mitochondria, yet integrated nuclear membrane prevented its entry, resulting in the decrease of the fluorescence in mitochondria.

Mechanism on Targeting and Localization Properties. To explain the mechanism that C3 targeted nucleolus in apoptotic cells, the interaction of C3 with RNA (nuclear acids) was preliminarily performed by single-photon fluorescent and two-photon fluorescent spectra. Such interactions will be strengthened upon the specific binding to the complementary target RNA (Figure 8), thus resulting in a “turn-on” effect.

To confirm that C3 was internalized with RNA, 1H NMR titration experiments were performed (Figure 8c). The protons Ha (Ha, Ha', Ha'', and Ha''') and Hb (Hb, Hb', Hb'', and Hb''') of the pyridine ring were upfield-shifted, and the signal intensity gradually weakened after titrating RNA, which suggested the H around C—C bond provided the possible binding sites for RNA. In combination with the optical properties, C3 and RNA interactions might affect the electronic distribution in the molecule.

Further molecular docking explained the mechanism of C3 binding to RNA. Evidently, C3 could insert duplex RNA (Figure 8d), which is consistent with the fluorescence titration experiments. It also indicated that the hydrogen bonds between C3 and RNA are derived from terpyridine groups and RNA base pairs.

All of these explorations suggested that probe C3 primarily served as a selective two-photon probe for apoptotic cells. It was confirmed that C3 showed a significant emission enhancement with RNA addition. Such result is critical, since mitochondrial RNA-based metal probes were rarely reported. It is known that RNA including tRNA (tRNA), mRNA (mRNA), and rRNA (rRNA) can be found in cytosol, mitochondria, and nucleolus. C3 thus offered a tool to investigate their dynamic change during apoptotic process, with high biocompatibility and photon stability. Related studies were undertaken and will be reported in further publication.

CONCLUSIONS

In conclusion, three Zn(II) complexes with 2PA were synthesized and confirmed through single-crystal X-ray diffraction analysis. With slight modification of the terminal substituent, these zinc complexes had obvious changes in the photophysical performance. The moderate 2PA activity as well as high cell viability of the Zn(II) complex make C3 a promising tool for bioimaging applications. 2PM and TEM images established that C3 initially localized to the mitochondria and then moved to the nucleolus during apoptosis, possibly binding with RNA. The success of C3 should be attributed to the aborative adjusting of the chemical structure of organic cationic complexes. Furthermore, the real-time studies using 2PM demonstrated that C3 was able to act as an indicator for cell mortality at subcellular level. These results make C3 of interest as the basis to design a probe to

discriminate live and apoptotic cells from organelles differentiated fluorescence.

ASSOCIATED CONTENT

Supporting Information

The Supporting Information is available free of charge on the ACS Publications website at DOI: 10.1021/acs.inorgchem.8b00620.

Crystal data, photophysical properties, and characterization data of all the compounds (PDF)

Related fluorescence intensities and HeLa cells stained with C3 (AVI)

Accession Codes

CCDC 1534933, 1568681, 1570231, and 1587882 contain the supplementary crystallographic data for this paper. These data can be obtained free of charge via www.ccdc.cam.ac.uk/data_request/cif, or by emailing data_request@ccdc.cam.ac.uk, or by contacting The Cambridge Crystallographic Data Centre, 12 Union Road, Cambridge CB2 1EZ, UK; fax: +44 1223 336033.

AUTHOR INFORMATION

Corresponding Authors

*E-mail: yptian@ahu.edu.cn. (Y.-P.T.)

*E-mail: xiaohe.t@ahu.edu.cn. (X.-H.T.)

ORCID

Dandan Liu: 0000-0002-1584-9299

Wei Du: 0000-0002-7959-6227

Fei Li: 0000-0001-9822-7526

Xiaohe Tian: 0000-0002-2294-3945

Zhongping Zhang: 0000-0002-0991-7611

Author Contributions

D.D.L. and M.Z.Z. contributed equally to this work and should be considered as cofirst authors.

Notes

The authors declare no competing financial interest.

ACKNOWLEDGMENTS

This work was supported by a grant from the National Natural Science Foundation of China (51432001, 51672002, 21602003, 51772002, and 21501001), Anhui Provincial Natural Science Foundation of China (1708085MC68), and Anhui Univ. Doctor Startup Fund (J01001962), Returnees innovation and entrepreneurship key support program, Postdoctoral Science Foundation of Anhui Province (2016B092), China Postdoctoral Science Foundation (2017M612050). The Natural Science Foundation of Anhui Province (1508085MB34). Focus on returned overseas scholar of Ministry of Education of China, the Higher Education Revitalization Plan Talent Project (2013).

REFERENCES

- (1) Schubert, N.; Park, S. H.; Baek, K. H.; Namkung, W.; Sessler, J. L.; Gale, P. A.; Shin, I.; et al. A synthetic ion transporter that disrupts autophagy and induces apoptosis by perturbing cellular chloride concentrations. *Nat. Chem.* **2017**, *9*, 667–675.
- (2) Saita, S.; Nolte, H.; Fiedler, K. U.; Kashkar, H.; Venne, A. S.; Zahedi, R. P.; Krüger, M.; Langer, T. PARL mediates Smac proteolytic maturation in mitochondria to promote apoptosis. *Nat. Cell Biol.* **2017**, *19*, 318–328.

- (3) Ishihara, N.; Mihara, K. PARL paves the way to apoptosis. *Nat. Cell Biol.* **2017**, *19*, 263–265.
- (4) Thapa, B.; Bahadur KC, R.; Uludağ, H. Novel targets for sensitizing breast cancer cells to TRAIL-induced apoptosis with siRNA delivery. *Int. J. Cancer* **2018**, *142*, 597–606.
- (5) Visan, I. Apoptosis footprint. *Nat. Immunol.* **2017**, *18*, 14.
- (6) Guo, J. W.; Guan, P. P.; Wang, S. L.; Huang, X. S.; Wang, Z. Y.; Wang, P.; et al. Erythrocyte membrane-encapsulated celecoxib improves the cognitive decline of Alzheimer's disease by concurrently inducing neurogenesis and reducing apoptosis in APP/PS1 transgenic mice. *Biomaterials* **2017**, *145*, 106–127.
- (7) Castro, R. E.; Santos, M. M. M.; Gloria, P. M. C.; Ribeiro, C. J. A.; Ferreira, D. M. S.; Xavier, J. M.; Moreira, R.; Rodrigues, C. M. P. Cell death targets and potential modulators in Alzheimer's disease. *Curr. Pharm. Des.* **2010**, *16*, 2851–2864.
- (8) Obulesu, M.; Lakshmi, M. J. Apoptosis in Alzheimer's disease: an understanding of the physiology, pathology and therapeutic avenues. *Neurochem. Res.* **2014**, *39*, 2301–2312.
- (9) Liu, Y.; Wu, P.; Jiang, J. H.; Wu, J. T.; Chen, Y.; Tan, Y.; Tan, C. Y.; Jiang, Y. Y. Conjugated Polyelectrolyte Nanoparticles for Apoptotic Cell Imaging. *ACS Appl. Mater. Interfaces* **2016**, *8*, 21984–21989.
- (10) Li, X. C.; Tian, M. G.; Zhang, G.; Guo, L. F.; Yu, X. Q.; Zhao, N.; He, X. Q.; et al. Spatially Dependent Fluorescent Probe for Detecting Different Situations of Mitochondrial Membrane Potential Conveniently and Efficiently. *Anal. Chem.* **2017**, *89*, 3335–3344.
- (11) Bui, A. T.; Beyler, M.; Liao, Y. Y.; Guennic, B. L.; Andraud, C.; Maury, O.; Tripier, R.; et al. Cationic Two-Photon Lanthanide Bioprobes Able to Accumulate in Live Cells. *Inorg. Chem.* **2016**, *55*, 7020–7025.
- (12) Lozano-Torres, B.; Galiana, I.; Rovira, M.; Garrido, E.; Chaib, S.; Bernardos, A.; Muñoz-Espín, D.; Serrano, M.; Martínez-Máñez, R.; Sanecnón, F. An OFF-ON Two-Photon Fluorescent Probe for Tracking Cell Senescence in Vivo. *J. Am. Chem. Soc.* **2017**, *139*, 8808–8811.
- (13) Tang, J.; Zhang, Y. F.; Yin, H. Y.; Zhang, J. L.; et al. Precise Labeling and Tracking of Lipid Droplets in Adipocytes Using a Luminescent ZnSalen Complex. *Chem. - Asian J.* **2017**, *12*, 2533–2538.
- (14) Tang, J.; Yin, H. Y.; Zhang, J. L. A luminescent aluminium salen complex allows for monitoring dynamic vesicle trafficking from the Golgi apparatus to lysosomes in living cells. *Chem. Sci.* **2018**, *9*, 1931–1939.
- (15) Liu, Z. P.; He, W. J.; Guo, Z. J. Metal coordination in photoluminescent sensing. *Chem. Soc. Rev.* **2013**, *42*, 1568–1600.
- (16) Tan, J. C.; Cheetham, A. K. Mechanical properties of hybrid inorganic-organic framework materials: establishing fundamental structure-property relationships. *Chem. Soc. Rev.* **2011**, *40*, 1059–1080.
- (17) Green, K. A.; Cifuentes, M. P.; Samoc, M.; Humphrey, M. G. Metal alkynyl complexes as switchable NLO systems. *Coord. Chem. Rev.* **2011**, *255*, 2530–2541.
- (18) Shewring, J. R.; Cankut, A. J.; McKenzie, L. K.; Botchway, S. W.; Weinstein, J. A.; Edwards, E.; Ward, M. D.; et al. Multimodal Probes: Superresolution and Transmission Electron Microscopy Imaging of Mitochondria, and Oxygen Mapping of Cells, Using Small-Molecule Ir(III) Luminescent Complexes. *Inorg. Chem.* **2017**, *56*, 15259–15270.
- (19) Gao, Y. H.; Wu, J. Y.; Li, Y. M.; Sun, P. P.; Zhou, H. P.; Yang, J. X.; Zhang, S. L.; Jin, B. K.; Tian, Y. P. A sulfur-terminal Zn (II) complex and its two-photon microscopy biological imaging application. *J. Am. Chem. Soc.* **2009**, *131*, 5208–5213.
- (20) Tang, J.; Yin, H. Y.; Zhang, J. L. Luminescent Zinc Complexes as Bioprobes for Imaging Molecular Events in Live Cells. *Inorganic and Organometallic Transition Metal Complexes with Biological Molecules and Living Cells*; Academic Press, 2017; pp 1–53. DOI: 10.1016/B978-0-12-803814-7.00001-0
- (21) Tang, J.; Cai, Y. B.; Jing, J.; Zhang, J. L. Unravelling the correlation between metal induced aggregation and cellular uptake/subcellular localization of ZnSalen: an overlooked rule for design of luminescent metal probes. *Chem. Sci.* **2015**, *6*, 2389–2397.
- (22) Tian, X. H.; Zhang, Q.; Zhang, M. Z.; Wu, J. Y.; Tian, Y. P.; et al. Probe for simultaneous membrane and nucleus labeling in living cells and in vivo bioimaging using a two-photon absorption water-soluble Zn(II) terpyridine complex with a reduced π -conjugation system. *Chem. Sci.* **2017**, *8*, 142–149.
- (23) Hu, J. Y.; Wu, Z. Y.; Chai, K.; Yang, Z. S.; Meng, Y. S.; Ning, Y. Y.; Zhang, J.; Zhang, L. J. β -Fluorinated porpholactones and metal complexes: synthesis, characterization and some spectroscopic studies. *Inorg. Chem. Front.* **2017**, *4*, 1539–1545.
- (24) Jung, H. S.; Lee, J. H.; Kim, K.; Koo, S.; Verwilt, P.; Sessler, J. L.; Kang, C.; Kim, J. S. A Mitochondria-Targeted Cryptocyanine-Based Photothermogenic Photosensitizer. *J. Am. Chem. Soc.* **2017**, *139*, 9972–9978.
- (25) Lincoln, R.; Greene, L. E.; Zhang, W. Z.; Louisia, S.; Cosa, G. Mitochondria Alkylation and Cellular Trafficking Mapped with a Lipophilic BODIPY-Acrolein Fluorogenic Probe. *J. Am. Chem. Soc.* **2017**, *139*, 16273–16281.
- (26) Whittle, B.; Horwood, E. L.; Ward, M. D.; et al. Crystal structures of a series of Co^{II}, Cu^{II} and Zn^{II} complexes of 4'-(3,4-dihydroxyphenyl)-2,2':6',2''-terpyridine and 4'-(3,4-dimethoxyphenyl)-2,2':6',2''-terpyridine. *Polyhedron* **1998**, *17*, 373–379.
- (27) Zou, H. H.; Wang, L.; Long, Z. X.; Chen, Z. F.; et al. Preparation of 4-([2,2':6',2''-terpyridin]-4'-yl)-N,N-diethylaniline Ni^{II} and Pt^{II} complexes and exploration of their in vitro cytotoxic activities. *Eur. J. Med. Chem.* **2016**, *108*, 1–12.
- (28) Grabowski, Z. R.; Rotkiewicz, K.; et al. Structural changes accompanying intramolecular electron transfer: focus on twisted intramolecular charge-transfer states and structures. *Chem. Rev.* **2003**, *103*, 3899–4031.
- (29) Tang, Y. W.; Kong, M.; Tian, X. H.; Wang, J. H.; Xie, Q. Y.; Wang, A. D.; Zhang, Q.; Zhou, H. P.; Wu, J. Y.; Tian, Y. P. A series of terpyridine-based zinc (ii) complexes assembled for third-order nonlinear optical responses in the near-infrared region and recognizing lipid membranes. *J. Mater. Chem. B* **2017**, *5*, 6348–6355.
- (30) Schlutter, F.; Wild, A.; Winter, A.; Hager, M. D.; Baumgaertel, A.; Friebe, C.; Schubert, U. S. Synthesis and characterization of new self-assembled metallo-polymers containing electron-withdrawing and electron-donating bis (terpyridine) zinc (II) moieties. *Macromolecules* **2010**, *43*, 2759–2771.
- (31) Shi, F. P.; Coe, B. J.; Wang, D. Q.; Tian, Y. P.; Nyk, M.; Samo, M.; et al. Uniting Ruthenium(II) and Platinum(II) Polypyridine Centers in Heteropolymetallic Complexes Giving Strong Two-Photon Absorption. *Inorg. Chem.* **2015**, *54*, 11450–11456.
- (32) Morrall, J. P.; Dalton, G. T.; Humphrey, M. G.; Samoc, M. Organotransition Metal Complexes for Nonlinear Optics. *Adv. Organomet. Chem.* **2007**, *55*, 61–136.
- (33) Chekeni, F. B.; Elliott, M. R.; Sandilos, J. K.; Walk, S. F.; Kinchen, J. M.; Lazarowski, E. R.; Armstrong, A. J.; Penuela, S.; Laird, D. W.; Salvesen, G. S.; et al. Pannexin 1 channels mediate 'find-me' signal release and membrane permeability during apoptosis. *Nature* **2010**, *467*, 863–867.
- (34) Weaver, R. F. *Molecular Biology*; McGraw-Hill Education, 2011.
- (35) Kim, H. M.; Cho, B. R. Small-molecule two-photon probes for bioimaging applications. *Chem. Rev.* **2015**, *115*, 5014–5055.